

## RESEARCH ARTICLE

10.1002/2014JB011289

## Key Points:

- Rupture processes of the 1980, 1997, 2009, and 2013 large Vanuatu earthquakes
- Analysis of the relationship between these large Vanuatu earthquake sequences
- Doublet and aftershock expansion related to asperity interaction

## Supporting Information:

- Readme
- Table S1 and Figures S1–S15
- Figure S16
- Figure S17
- Figure S18

## Correspondence to:

K. M. Cleveland,  
mike.cleveland@gmail.com

## Citation:

Cleveland, K. M., C. J. Ammon, and T. Lay (2014), Large earthquake processes in the northern Vanuatu subduction zone, *J. Geophys. Res. Solid Earth*, 119, 8866–8883, doi:10.1002/2014JB011289.

Received 14 MAY 2014

Accepted 31 OCT 2014

Accepted article online 6 NOV 2014

Published online 3 DEC 2014

## Large earthquake processes in the northern Vanuatu subduction zone

K. Michael Cleveland<sup>1,2</sup>, Charles J. Ammon<sup>1</sup>, and Thorne Lay<sup>3</sup>

<sup>1</sup>Department of Geosciences, Pennsylvania State University, University Park, Pennsylvania, USA, <sup>2</sup>EES-17, Geophysics, Los Alamos National Laboratory, Los Alamos, New Mexico, USA, <sup>3</sup>Earth and Planetary Sciences Department, University of California, Santa Cruz, California, USA

**Abstract** The northern Vanuatu (formerly New Hebrides) subduction zone (11°S to 14°S) has experienced large shallow thrust earthquakes with  $M_w > 7$  in 1966 ( $M_s$  7.9, 7.3), 1980 ( $M_w$  7.5, 7.7), 1997 ( $M_w$  7.7), 2009 ( $M_w$  7.7, 7.8, 7.4), and 2013 ( $M_w$  8.0). We analyze seismic data from the latter four earthquake sequences to quantify the rupture processes of these large earthquakes. The 7 October 2009 earthquakes occurred in close spatial proximity over about 1 h in the same region as the July 1980 doublet. Both sequences activated widespread seismicity along the northern Vanuatu subduction zone. The focal mechanisms indicate interplate thrusting, but there are differences in waveforms that establish that the events are not exact repeats. With an epicenter near the 1980 and 2009 events, the 1997 earthquake appears to have been a shallow intraslab rupture below the megathrust, with strong southward directivity favoring a steeply dipping plane. Some triggered interplate thrusting events occurred as part of this sequence. The 1966 doublet ruptured north of the 1980 and 2009 events and also produced widespread aftershock activity. The 2013 earthquake rupture propagated southward from the northern corner of the trench with shallow slip that generated a substantial tsunami. The repeated occurrence of large earthquake doublets along the northern Vanuatu subduction zone is remarkable considering the doublets likely involved overlapping, yet different combinations of asperities. The frequent occurrence of large doublet events and rapid aftershock expansion in this region indicate the presence of small, irregularly spaced asperities along the plate interface.

## 1. Introduction

The northern Vanuatu subduction zone (11°S to 14°S) has experienced numerous moderate-to-large earthquakes in the past few decades (Figure 1); however, no events exceeding  $M \sim 8.0$  are listed for this region in earthquake catalogs dating back to 1900 [Allen *et al.*, 2009]. There is no guarantee that the maximum viable earthquake for the region has been observed in the relatively short duration seismological record; a synchronous multiple-segment rupture, which could result in a larger earthquake than those recorded to date, cannot be ruled out for the future. The high rate of moderate magnitude seismicity in the region over the last 50 years has been punctuated by five sequences of major earthquakes in 1966, 1980, 1997, 2009, and 2013 (Figure 2).

The 31 December 1966 earthquake sequence included two large events in 4 h. The first event occurred at 18:23:08.8 UTC ( $M_s$  7.9, 11.9°S 166.4°E), followed by an  $M_s$  7.3 aftershock at 22:15:17.1 UTC (12.1°S 165.7°E) [Tajima *et al.*, 1990]. While the International Seismological Centre catalog (ISC) lists a depth of 73 km for the first event, Tajima *et al.* [1990] found that the long-period surface wave observations were most consistent with a depth of  $\sim 40$  km. They were unable to fully constrain the 1966 faulting geometry using  $P$  wave first-motion data but suggested a similar faulting geometry to the 17 July 1980 event (strike,  $\phi = 347^\circ$ , dip,  $\delta = 36^\circ$ , and rake,  $\lambda = 91^\circ$ ). Short-arc Rayleigh wave (R1) directivity information suggests that the larger 1966 event ruptured unilaterally to the north along strike [Tajima *et al.*, 1990] and the peak energy release rate occurred between 12 and  $\sim 50$  s after the rupture initiation. The rupture pattern suggests that a barrier may have blocked rupture propagation to the south [Tajima *et al.*, 1990]. The aftershock pattern extended almost exclusively to the north and was characterized by rapid areal expansion, spanning a region  $\sim 200$  km wide. The 100 day aftershock region was more than 3 times larger than the 1 day region; Tajima and Kanamori [1985] note that the western Pacific characteristically exhibits significant aftershock expansion rates, possibly reflecting a lower density of asperities. Smaller events later ruptured in the region south of the 1966 seismicity on 23 January 1972 ( $M_s$  7.1, 13.2°S 166.3°E) and 6 October 1975 ( $M_s$  7.0, 12.5°S 166.6°E).

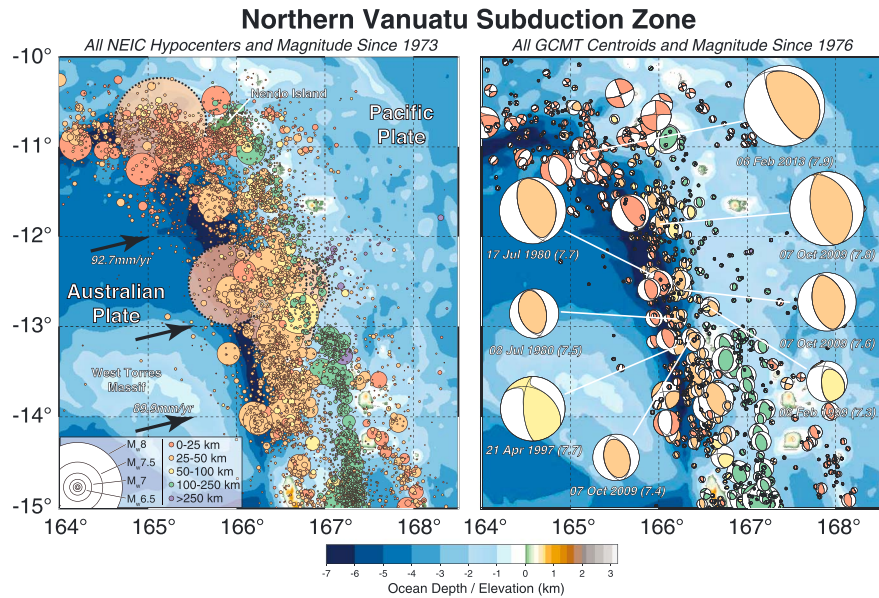


**Figure 1.** (left) Seismicity of the northern Vanuatu subduction zone, displaying all USGS-NEIC earthquake hypocenters since 1973. The Australian plate subducts beneath the Pacific in nearly trench-orthogonal convergence along the Vanuatu subduction zone. The largest events are displayed with dotted outlines of the magnitude-scaled circle. Convergence rates are calculated using the MORVEL model for Australia Plate relative to Pacific Plate [DeMets *et al.*, 2010]. (right) All GCMT moment tensor solutions and centroids for  $M_w \geq 5$  since 1976, scaled with moment. This region experiences abundant moderate and large earthquakes but lacks any events with  $M_w > 8$  since at least 1900.

The strike of the 1972 event was rotated slightly more to the east of the 1966 events. The aftershock area of the 1972 event did not expand much beyond the 1 day region, remaining under  $\sim 125$  km in extent [Tajima and Kanamori, 1985]. As will be discussed later, while the 2009 and 2013 earthquakes ruptured near the 1966 seismicity region, it does not appear the large-slip zone reruptured.

The 1980 sequence (Figure 2) began on 8 July 1980 with an  $M_w$  7.5 thrust event ( $12.92^\circ\text{S}$   $166.21^\circ\text{E}$ , 43.6 km) and was followed about a week later by a larger thrust event ( $M_w$  7.7) on 17 July 1980 ( $12.44^\circ\text{S}$   $165.94^\circ\text{E}$ , 34.0 km). While some consider the first event a foreshock, Tajima and Kanamori [1985] noted that this event

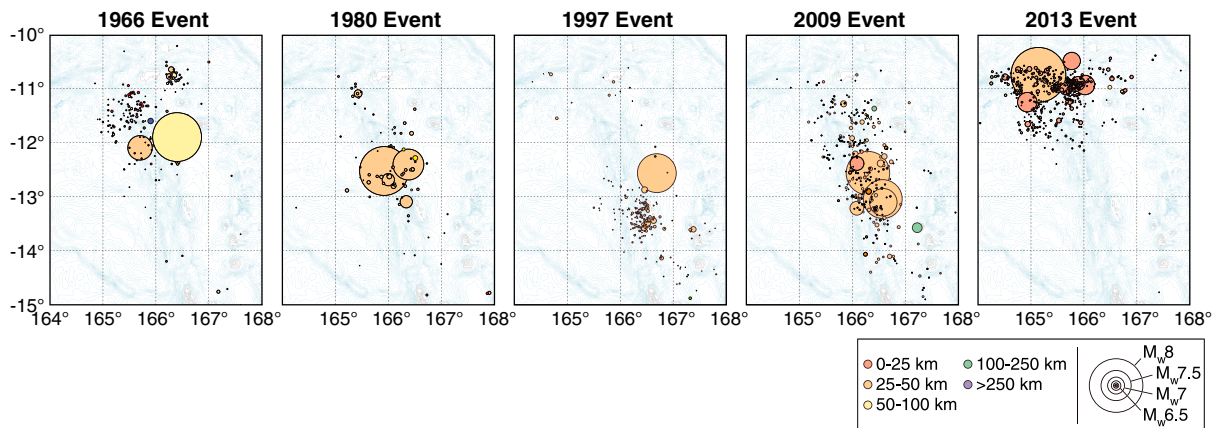


**Figure 2.** One hundred day aftershock distributions of all earthquakes listed in the ISC catalog for the 1966 sequence and in the USGS-NEIC catalog for the 1980, 1997, 2009, and 2013 sequences in northern Vanuatu. The 1966 main shocks are plotted at locations listed by Tajima *et al.* [1990]. Events of the 1997 and 2009 sequences were relocated using the double difference method [Waldhauser and Ellsworth, 2000] for P wave first arrivals based on EDR picks. The event symbol areas are scaled relative to the earthquake magnitudes based on a method developed by Utsu and Seki [1954]. Hypocenters of most aftershock events occurred at  $< 50$  km depth.

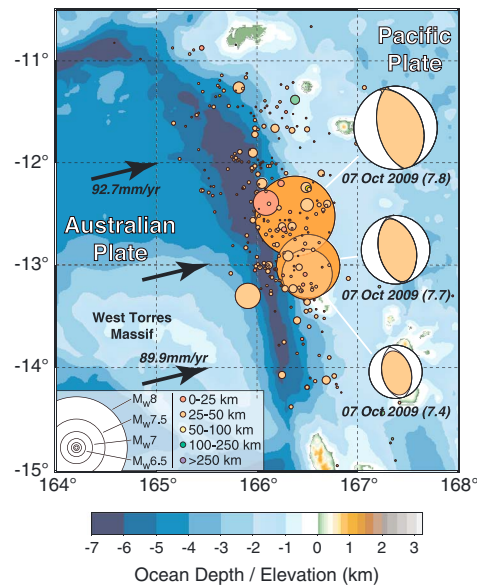


**Figure 3.** The 7 October 2009 large earthquake triplet in the northern Vanuatu subduction zone and its 3 month aftershock sequence ( $M_w > 4$ ). The sequence began with the  $M_w$  7.7 event, followed ~15 min later by the  $M_w$  7.8 event, and about an hour later the  $M_w$  7.4 event. The circles indicate NEIC epicenters and the focal mechanisms are from GCMT. Convergence rates are calculated using the MORVEL model [DeMets et al., 2010].

of the 1966 1 day aftershock area. The 17 July 1980 event ruptured within the aftershock region of the first 1980 event. The northern extent of this aftershock 100 day area also overlapped the 1966 aftershock region [Tajima et al., 1990]. Estimates by Tajima et al. [1990] suggest that the source area of the 1980 events was twice as large as the 1966 sequence, but the seismic slip was only half as great as the former event. There was no appreciable expansion in the aftershock area following the 17 July 1980 event [Tajima and Kanamori, 1985]. We infer that the coseismic slip zones of the 1980 sequence did not overlap that of the 1966 events, although seismicity was induced at latitudes from 11°S to 11.5°S by both sequences.

A single large earthquake ruptured slightly south of the 1980 sequence on 21 April 1997 ( $M_w$  7.7 13.21°S 166.20°E), producing a local tsunami reported as high as 3 m in the Solomon and Vanuatu islands [Kaverina et al., 1998]. The GCMT best double-couple mechanism ( $\phi = 301^\circ$ ,  $\delta = 39^\circ$ , and  $\lambda = 40^\circ$ ) of this event has a strike rotated slightly more toward the northwest than the 1966 and 1980 sequences, but similar dip. Analysis of S and SS waves using an empirical Green's function method led Kaverina et al. [1998] to suggest that the hypocenter was deep but the peak slip of 4.25 m occurred between shallow depths of 5 to 20 km, updip and to the south of the origin. The GCMT and W-Phase solutions (G. Hayes, personal communication, 2011) also indicate a deep centroid of 45 km for this event. The aftershock sequence of this event was shallow and near the trench (Figure 2).

On 7 October 2009, ~350 km of the northern extent of the Vanuatu subduction zone ruptured in three major, shallow thrust earthquakes (Figures 2 and 3) with similar centroids to the 1980 doublet. The first 2009 event occurred at 22:03:15 UTC (National Earthquake Information Center (NEIC):  $M_w$  7.7, 13.052°S 166.187°E), followed 15 min later by a slightly larger event (NEIC:  $M_w$  7.8, 12.554°S 166.320°E, 22:18:26 UTC). A third major earthquake in the sequence occurred about an hour after the first (NEIC:  $M_w$  7.4, 13.145°S 166.297°E, 23:13:49 UTC). A modestly damaging tsunami with peak water height of 0.1–0.3 m on tide gauges in the Vanuatu islands (south of the region shown in Figure 3) was associated with this sequence (National Oceanic and Atmospheric Administration (NOAA) GCMT mechanisms indicate that all of the events in this sequence ruptured similarly oriented faults. Widespread aftershock activity occurred, again including events in the range 11°S to 11.5°S.

(8 July 1980) produced its own aftershocks, indistinguishable from those of the latter, larger event (17 July 1980), leading them to interpret both as main shocks. Both events of this sequence displayed similar focal mechanisms compatible with the 1966 main shock (Global Centroid Moment Tensor (GCMT) <http://www.globalcmt.org>) [e.g., Ekström et al., 2012; Tajima et al., 1990]. The moment rate function of the 17 July 1980 event was complex with peaks occurring around 30 and 60 s. Rupture modeling using body waveform inversion suggests that the primary rupture occurred in the downdip portion of the seismogenic zone. In the first ~30 s, most of the moment release occurred just south of the epicenter. Following the initial 30 s, rupture occurred primarily to the north [Tajima et al., 1990]. Tajima et al. [1990] suggested that the 1980 sequence represents the failure of the asperity that served as a barrier to the southern propagation of the 1966 event.

The aftershock pattern of the 1980 sequence expanded substantially toward the north, encompassing the 1966 aftershock zone. The 100 day aftershock area was more than 3 times the size of the 1 day region [Tajima and Kanamori, 1985]. The 1 day aftershock area of the 8 July 1980 event included part of the aftershock area of the moderate size 1972 and 1975 events and extended up to the southern boundary

Most recently, the 6 February 2013 (NEIC:  $M_w$  8.0, 10.738°S, 165.138°E) great earthquake ruptured a fault segment just north of the 1966 sequence (Figure 2). The 2013 main shock hypocenter is over 150 km north of the 1966 hypocenters; however, the aftershock zones overlap in the repeatedly activated zone from 11°S to 11.5°S. *Hayes et al.* [2014] infer that slow slip occurred down-dip on the megathrust in this zone during the 2013 sequence. The frictional coupling in this region appears distinct from the megathrust to the north and to the south. The 2013 earthquake produced a local tsunami as high as 3 m on Nendö Island (NOAA). The GCMT faulting parameters ( $\phi = 314^\circ$ ,  $\delta = 21^\circ$ , and  $\lambda = 74^\circ$ ) indicate that the 2013 event had similar faulting geometry to the 1966, 1980, and 2009 sequences. This is the largest event recorded for the northern Vanuatu region [e.g., *Lay et al.*, 2013].

Globally, large earthquake doublets have been observed in several regions [e.g., *Lay and Kanamori*, 1980; *Kagan and Jackson*, 1999; *Felzer et al.*, 2004; *Ammon et al.*, 2008; *Lay et al.*, 2010a]. The northern Vanuatu region is similar to the Solomon Islands in having an unusual number of large doublets and triplets (Figure 2). This may reflect greater triggering efficiency in these regions. In this study, we analyze the body and surface waves generated by the large earthquakes in 1980, 1997, 2009, and 2013. We extend previous work by others on the 1980 events and the 1997 rupture (the digital data available for the 1980 sequence are limited). We find that each sequence appears to have ruptured partially overlapping regions of the plate boundary (and within the slab in 1997). Clarifying the relationships of large related earthquakes is an important part of the long-term effort to understand large earthquake interactions. Analysis of these interactions and comparison of characteristics of each sequence (e.g., aftershock patterns and rupture characteristics) can help constrain the regional plate coupling and plate interface morphology. We begin by describing the 2009 sequence and its relationship to the 1980 sequence, then describe the 1997 and 2013 earthquakes, and conclude by discussing the overall large earthquake process in the northern Vanuatu subduction zone.

## 2. The 2009 Earthquake Sequence

The short, 15 min time separation between the two largest 2009 events complicates seismic wave analyses, but we are able to constrain important aspects of each of the ruptures. We used global broadband R1 waves to estimate the overall rupture characteristics of each event. Specifically, we deconvolved point source seismograms with aspherical Earth model fundamental mode phase corrections from group velocity-windowed observed seismograms. We used both iterative time domain [*Kikuchi and Kanamori*, 1982] and water level approaches to remove propagation effects to estimate the R1 source time function (STF). We present the results of the iterative approach and often for simplicity assume a uniform velocity (ignoring intrarupture dispersion) in our first-order calculations. For a detailed discussion of the method, see *Ammon et al.* [2006] and *Lay et al.* [2010a].

Due to the short interval between the two 2009 events, we deconvolved synthetic point source seismograms from the observed composite R1 recordings. For stations at closer distances, the two R1 wave trains are reasonably well isolated and we can confidently estimate the R1 STFs for both events. At larger distances, R1 from the earlier event is contaminated by multibounce S waves from the second event, limiting the number of useful STFs for the first event. R1 for the second event is generally clear of major interference. The resulting R1 STFs for the two events are shown in Figure 4. We show STFs computed with a positivity constraint in a time domain iterative deconvolution, but we also examined STFs obtained using a water level deconvolution (which are consistent but slightly noisier than those presented). Although the Green's functions include periods as short as 20 s, the STFs contain reliable source information in the period range from about 50 to 200 s. These signals constrain aspects of the overall rupture process, such as rupture direction and duration, but provide only weak resolution of rupture speed.

The R1 STFs from the first event are displayed in Figure 4 as a function of the directivity parameter  $\Gamma$ , which was computed assuming that the rupture direction is along the trench strike (the directivity parameter is the product of the wave horizontal slowness and the cosine of the difference between the observation and the rupture azimuths). We only used R1 STFs that produced at least an 80% fit to the convolutional model (STF convolved with the Green's function should reproduce the observed signal). As a result of event interference, only several dozens out of nearly 300 observed waveforms met this standard, and the results are noisy, but they provide a sufficient azimuthal sampling. The STFs vary slightly but show no consistent directivity effect. The lack of directivity is an indication of a relatively compact, possibly bilateral rupture.

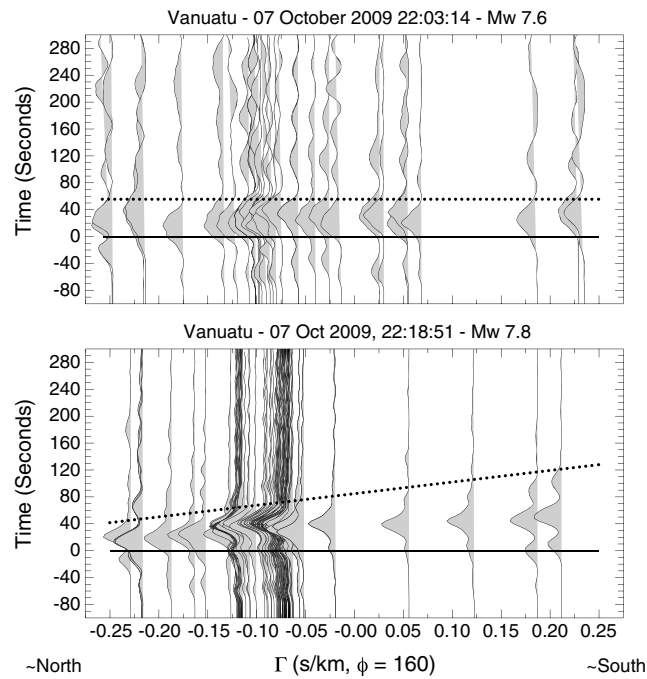


**Figure 4.** R1 source time functions (STFs) for the (top) first and (bottom) second large 2009 earthquakes plotted versus directivity parameter,  $\Gamma$ , for an assumed rupture azimuth of  $160^\circ$ . The STFs are aligned by R1 arrival (solid black line). The dotted black line shows the best fitting moveout trend based on visual inspection. The first rupture shows little evidence of directivity and appears to have about 40–50 s duration. The second rupture appears to propagate to the north ( $N340^\circ$ , with narrow pulses in the negative directivity parameter direction) with an estimated rupture speed of about 2.1 km/s and an  $\sim 80$  s duration.

to the south (away from the rupture propagation) suggest that the rupture included at least two and perhaps three significant subevents. STFs at azimuths orthogonal to the rupture direction are simple and indicate that the rupture had a total duration of about 80 s. A substantial peak in moment rate occurred at 40 s with a large, slightly asymmetric pulse. The third subevent apparent in the STFs to the south appears to have occurred close in time to the large pulse. Assuming a simple, unilateral rupture and an average R1 phase velocity of about 4 km/s, the roughly 85 s of directivity indicates a rupture length of about 170 km; the estimated rupture speed is  $\sim 2.1$  km/s, but this estimate might be biased as a result of the broadening of the STFs by the low-pass Gaussian filter applied to the STF estimates. Assuming a maximum broadening of 30 s would lead to a rupture speed estimate of 3.6 km/s (the broadening does not affect the length estimate because that is based on a difference in durations). Our resolution is limited, but analysis of the STFs and results from finite-fault modeling described next lead us to believe that the true velocity is closer to the lower rupture speed estimate than the higher.

We use teleseismic broadband *P* and *SH* waves in a finite-fault inversion to provide more information on the rupture characteristics of the first event. We applied the finite-fault modeling procedure of M. Kikuchi and H. Kanamori to invert teleseismic body waves using a kinematic-constrained linear least squares procedure and a layered Earth model. We performed a grid search to identify optimal values for hypocenter depth, dip, and strike. Specifically, we varied the strike between  $342^\circ$  and  $354^\circ$ , and the dip from  $42^\circ$  to  $48^\circ$ , and tested hypocenter depths between 20 and 50 km. We also tested the auxiliary focal plane over comparable ranges of dip and depth for strike angles between  $166^\circ$  and  $175^\circ$ . The waveforms are best fit with a hypocenter depth of 39 km, rupture speed of 2.5 km/s, and focal parameters of  $\phi = 346^\circ$ ,  $\delta = 45^\circ$ , and  $\lambda = 86^\circ$ . Subfault source time functions were parameterized by eight half-overlapping, 1.5 s wide triangles. Smoothing was applied to produce the simplest model with an acceptable fit to the observations, and the data (and Green's functions) were filtered using a Butterworth filter to emphasize signal periods between

Including the broadening effects from the low-pass Gaussian filter, the duration of the event at stations nearly perpendicular to the assumed along-strike rupture direction is, at a maximum, about 50–60 s. The moment rate function shape is roughly symmetric. The Gaussian filter width is about 30 s (the width where the Gaussian amplitude is equal to 10% of its peak amplitude), but the amount of measurable broadening produced by the filter depends on the shape of the signal to which the filter is applied. A smooth function with a long rise time compared with the Gaussian duration is extended little by the filter. But a sharp, rise, or end of an STF is extended by roughly half the width of the Gaussian. In this case, our resolution is limited and the duration could have been up to 30 s shorter than the 50–60 s pulse width.

The STFs for the second event have much more variation, including  $\sim 85$  s of directivity. From the azimuthal directivity pattern, the second rupture appears to have propagated along strike toward the north ( $N340^\circ$ ). The temporally stretched STFs observed

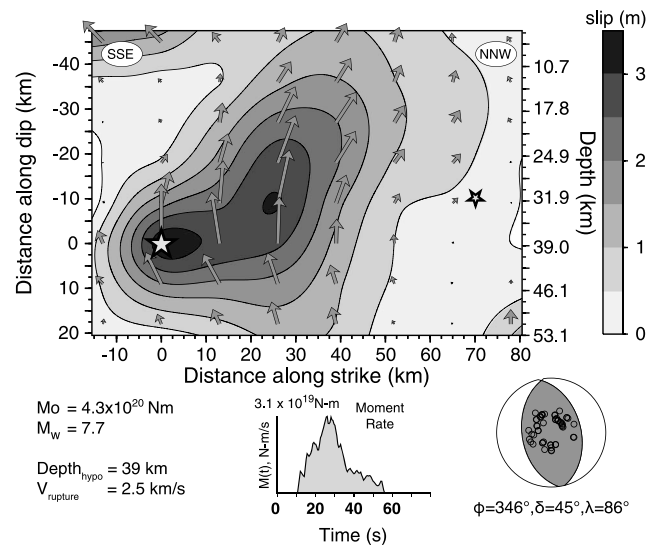


**Figure 5.** Finite-fault slip distribution from a kinematically constrained linear least squares inversion of teleseismic broadband *P* and *SH* waves for the first event in the 2009 sequence. The waveform fits are shown in Figure S1. The preferred mechanism is similar to the GCMT solution (strike = 344°, dip = 41°, and rake = 87°). The NEIC hypocenter of the second event in the sequence (inverted star on the right) is located north and slightly updip of the first (star on the left). The event had a peak slip of 3–4 m. A velocity boundary in our layered source structure enhances the along-dip gradient in slip just below the depth of the hypocenter.

estimate of  $3.3 \times 10^{20}$  N m. The model rupture speed is 2.5 km/s, which is well within the broad range compatible with the R1 STFs. Inversions with the fault model extending farther south also place the primary slip north of the hypocenter, so the northward propagation of the rupture is a robust feature constrained by the observations. The source time function duration is about 45 s, but moment release is skewed toward earlier times. The tail of the moment rate function would account for a 30% overestimation of moment and may simply reflect the difficulty of constraining a gradual decrease in moment rate using only body waves. The hypocenter of the second 2009 event is located just north of the rupture limit of this first event. Unfortunately, we are unable to perform a similar body wave analysis for the second, larger event, because the body waves are overwhelmed by signals from the earlier event.

To better define the relative rupture centroid positions for the three largest earthquakes in the 2009 sequence, we used a cross-correlation analysis of the R1 observations from each event. Because the rupture depths and the faulting geometry of all the events are similar, timing relations between the R1 waves can be used to obtain good estimates of the relative centroid locations for each event. Effectively, we cross-correlated signals from the first event with those from the second and third events and then fit a sinusoid to the resulting azimuthal patterns of phase shifts (Figure 6). This method does not provide information on the absolute location of the events; the entire pattern can be shifted without affecting the fit to the relative traveltimes observations. The later 2009 events were repositioned relative to a location based on results of finite-fault analysis (Figure 5) for the first 2009 event. The observations suggest that the second event's temporal centroid was approximately 15.75 min later than the first and the third event's centroid was about 70.50 min after the first. The second event's spatial centroid is located about 70 km due north of the first and the third event's centroid was about 60 km due south. The timing and locations are generally consistent with the GCMT centroid estimates, except the GCMT centroid of the second event is about 10 km north and slightly to the west of our location while the GCMT centroid of the third event is slightly east of our location. We performed a similar analysis on the 1980 data and found that the centroid of the 17 July event occurred about 76 km away at an azimuth of 346° relative to the 8 July event. Unfortunately, as a result of having very few common stations between the 1980 and 2009 events, an attempt at computing relative centroid location between the two sequences was inconclusive.

1 and 200 s. The data were chosen to provide balanced azimuthal coverage and to sample a range of available takeoff angles available in teleseismic *P* waves.

The finite-fault inversion indicates that a majority of the moment originated from an asymmetric region with length ~60 km along strike and width ~50 km (Figure 5). The model shows that the event initiated impulsively near the downdip edge of the eventual rupture zone. The moment rate increased rapidly to a peak at about 15 s as the rupture front expanded ~15 km to the north and then expanded in the updip direction. The fits to the waveforms are good (Figure S1 in the supporting information). There is little slip downdip of the hypocenter, but the rupture may extend to near the surface in the region NNW of the hypocenter. The peak slip is roughly 3–4 m and is largest within 10 km of the hypocenter. The model seismic moment is  $4.3 \times 10^{20}$  N m, which is about 30% larger than the GCMT

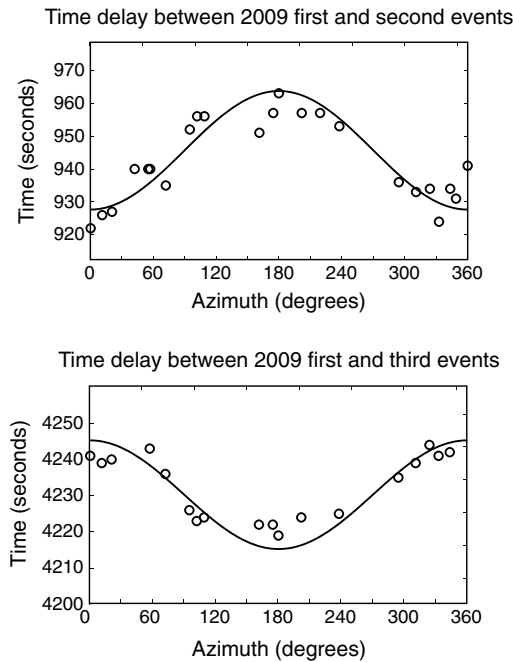


**Figure 6.** Azimuthal plots of the relative time delays between R1 arrivals for (top) the first and second events and (bottom) the first and third events. The time reference is the first 2009 event origin time. The mean time offset of the cosine curve indicates the difference in centroid time between the two events. The amplitude of the curve is a function of the distance between the two centroids, and the minima indicate the direction of the centroid of the second and third events relative to the first 2009 event.

To summarize the 2009 activity, the first event was relatively compact and ruptured a distance of about 60 km from south to north along the deeper region of the megathrust zone. The rupture began with a small, downdip subevent and ruptured northward into a larger asperity. About 15 min later, the second and larger earthquake occurred at the northern end of the first rupture. This event included at least two and perhaps three subevents and appears to have ruptured about 180 km to the north with an average rupture speed of about 2.1 km/s. A third event, with much smaller moment than the first two, occurred about 70 min later and was located to the south of the first event (Figure 2). Following these events, the entire length of the northern Vanuatu plate boundary quickly illuminated with seismic activity. The combined 1 day aftershock region extended ~300 km and over the following week extended to ~400 km along the plate boundary, with the main shock epicenters located roughly in the middle of this region (Figure 7). Aftershocks in the southern half of this region ceased after about 14 days, but those north of the large-event epicenters continued for nearly 2 months.

### 3. Waveform Comparison of the 1980 and 2009 Earthquake Sequences

Considering the 1980 and 2009 sequences, the locations, magnitudes, and similar faulting geometries of the largest events suggest that both of these pairs ruptured similar portions of the plate boundary. Given the close temporal proximity of the two largest 2009 events, it was not possible to effectively isolate either single event. Consequently, to compare the two sequences, we combined the two 1980 event waveforms with a best fitting offset to create a composite waveform to compare with the 2009 events. The composite of the 1980 events was created by determining the best fitting time offset and relative amplitude that minimized the L2 misfit to the 2009 time series. For completeness, we also investigated all doublet permutations of one or both 1980 events. The best fit was produced with a combination of the 8 July 1980 event waveform followed by the 17 July 1980 waveform (Figure 8). Because the waveforms from the second 1980 event were clipped at most stations, we included the instrument response

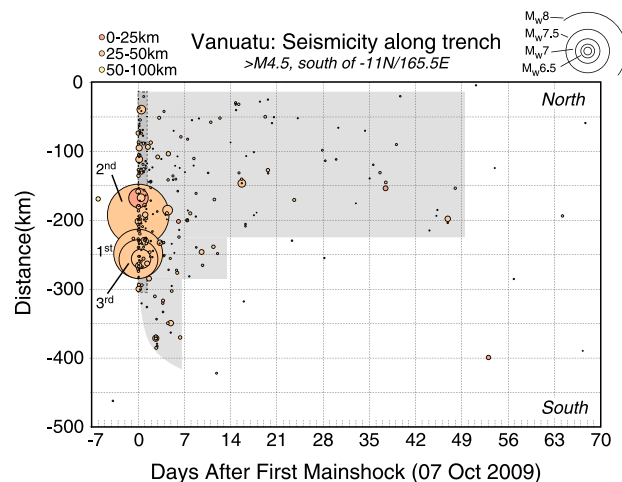


**Figure 7.** Space-time plot of the 7 October 2009 earthquake sequence. Distance is measured to the south from  $-11^{\circ}\text{N}$ ,  $165.5^{\circ}\text{E}$  along the strike of the trench. All events with NEIC magnitudes  $M > 4.5$  are displayed. Aftershock activity remained elevated for ~50 days following the main shock in the north but quickly dissipated south of this region. The initial rupture appears to have not extended very far south of the third event. However, aftershock activity displays a southern progression, before stopping after about a week.

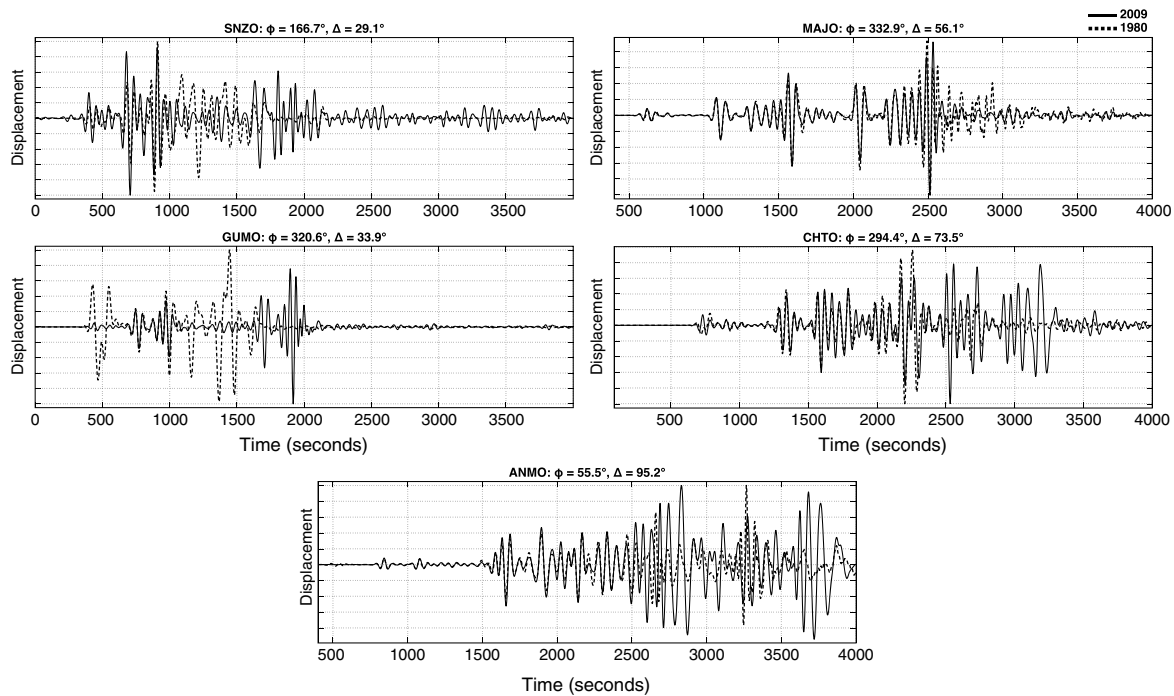


**Figure 8.** Long-period waveform matching of the October 2009 sequence (solid) and July 1980 (dashed). Given the close temporal proximity of the two largest 2009 events, it was not possible to effectively isolate a single event. Consequently, we combined the two 1980 main shocks with a best fitting offset to create a composite waveform, simulating the second 1980 event as having a similar time delay as for the second 2009 event.

of the 1980 earthquake's waveforms into the 2009 sequence's waveform and applied a causal low-pass filter to the second 1980 waveform. We can only reliably compare the waveforms prior to the arrival of the clipped R1 waves of the second 1980 event. This allows comparison of the entire initial 1980 event and the body waves of the second with the 2009 recordings.

The limited number of common stations, waveform quality, and azimuthal distribution restricted this analysis to only five stations: Albuquerque, NM ( $\phi = 55.5^\circ$ ,  $\Delta = 95.2^\circ$ , ANMO); Chiang Mai, Thailand ( $\phi = 294.4^\circ$ ,  $\Delta = 73.5^\circ$ , CHTO); Guam, Mariana Islands ( $\phi = 320.6^\circ$ ,  $\Delta = 33.9^\circ$ , GUMO); Matsushiro, Japan ( $\phi = 332.9^\circ$ ,  $\Delta = 56.1^\circ$ , MAJO); and South Karori, New Zealand ( $\phi = 166.7^\circ$ ,  $\Delta = 29.1^\circ$ , SNZO). Waveforms were low-pass filtered at 50 s. ANMO and MAJO stations are well fit up to  $\sim 2200$  and  $\sim 2500$  s, respectively. CHTO also provides a generally good match up to  $\sim 2500$  s; however, there is a notable difference in the first P wave arrival and at  $\sim 1800$  s. GUMO and SNZO generally display poor correlation between the two sequences, except the R1 waves of the first 1980 event appear to match well with the first 2009 event. Overall, the comparisons suggest that the events are similar but have some significant differences in radiation pattern, which suggests the two sequences are not exact repeats.

#### 4. The 1997 Earthquake

A number of issues are perplexing about the 1997 event. First, the long-period point source faulting geometry is significantly different from that of the large presumed underthrusting earthquakes in the region (Figure 1). Neither of the two planes aligns with the trench. Both GCMT and W-Phase inversions have small nondouble-couple components of the moment tensor, so there is no clear large-scale geometric complexity during faulting. Both long-period analyses also suggest a relatively deep centroid ( $\sim 45$  km). Additionally, a significant number of aftershocks in the sequence are offset to the south of the hypocenter and near the trench (Figure 2). Perhaps these aftershocks were triggered off fault; we investigate the event using analysis of the rupture.

To estimate the overall rupture characteristics of the 1997 event, we used similar analysis of R1 STFs as we used with the 2009 events. We assumed a point source with the GCMT faulting geometry ( $\phi = 301^\circ$ ,  $\delta = 39^\circ$ , and  $\lambda = 40^\circ$ ) and a depth of 45 km based on GCMT and W-Phase modeling (G. Hayes, personal

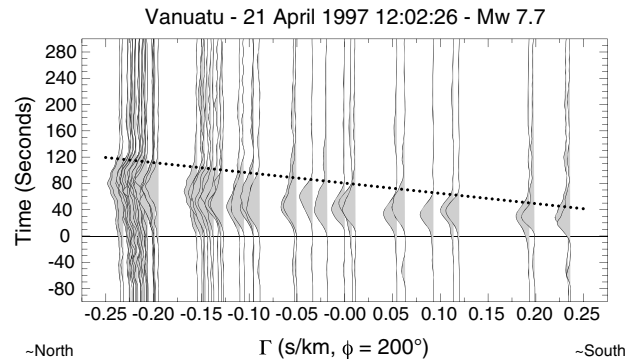


**Figure 9.** R1 source time functions (STFs) for the 1997 main shock plotted versus directivity parameter,  $\Gamma$ , for an assumed rupture azimuth of  $200^\circ$ . The rupture appears to be predominantly unilateral toward that azimuth and has an estimated rupture speed of 2.0 km/s and a 75–80 s faulting duration.

shown in Figure 9—the results are noisier but showed no systematic variations that would indicate a complex source [Lay et al., 2010b]. The STF ( $\Gamma = 0$ ) duration of about 75–80 s is somewhat longer than the 60–65 s duration of relative moment rate functions estimated using body waves for this event by Kaverina et al. [1998]. Considering that we have smoothed our estimates with the low-pass Gaussian filter, the difference is not significant. If we interpret the rupture as unilateral toward the  $200^\circ$  azimuth, we infer about 80 s of directivity (durations vary from 40 to 120 s). Assuming an R1 phase velocity of 4 km/s, the 80 s of directivity suggests a rupture length of about 160 km. The estimated rupture speed is about 2.0 km/s, but this estimate might be slightly low as a result of the Gaussian filter broadening of the STFs. The onset of the time functions is quite gradual, so if the Gaussian has introduced a bias, it would be primarily on the end of the rupture—assuming 15 s of Gaussian filter broadening suggests a rupture speed of about 2.5 km/s.

The R1 STFs are consistent with a rupture direction just west of south, generally toward the aftershock cluster. It is plausible that the event ruptured along a roughly west-southwest striking fault within the slab. Considering the dip of the descending lithosphere, the plane has about the orientation expected for a former transform fault or fracture zone that was initially near vertical in the oceanic lithosphere. Similar intraslab ruptures have been suggested as part of a complex  $M_w$  7.9 rupture near Sumatra [Abercrombie et al., 2003] and the 1986,  $M_w$  7.7, earthquake in the Kermedec region [Houston et al., 1993]. In each of these cases, the intraplate component of the earthquake was believed to be strike slip in nature, but both show that the strain retained within the downgoing slab is capable of producing substantial seismic events. On the other hand, Kaverina et al. [1998] tested the roughly north-south striking, steeply dipping plane in their analysis of body waves and found that they could fit their observations better by adjusting the dip of the complementary, shallower-dipping plane to have a more traditional subduction plate boundary orientation. However, that model does not account for the oblique geometry of the GCMT and W-phase solutions.

We used finite-fault inversions to estimate the slip distribution for the 1997 event for a number of rupture plane scenarios. The inversion was performed using similar methods as those used for the 2009 event.

**Table 1.** Rupture Models of 1997 Earthquake

Model	Strike ( $^\circ$ )	Dip ( $^\circ$ )	Rake ( $^\circ$ )	Depth (km)
GCMT-1 <sup>a</sup>	301	39	40	51
GCMT-2 <sup>a</sup>	178	66	122	51
Kaverina <sup>b</sup>	301	17	40	33
S200	200	66	122	51
S340	340	40	85	51

<sup>a</sup>Global Centroid Moment Tensor catalog.

<sup>b</sup>Kaverina et al. [1998].

communication, 2011). We examined the pattern of the relatively simple STF pulse shape duration as a function of assumed rupture directions. The most consistent pattern in STF pulse shape variation was observed for a rupture directed at an azimuth of  $200^\circ$  (Figure 9), which differs substantially from the trench strike ( $\sim 345^\circ$ ) but is not far from the orientation of the steeply dipping plane in the GCMT faulting geometry ( $178^\circ$ N) (although the general trend of long-versus short-duration STFs is similar for the  $178^\circ$  and  $200^\circ$  orientations,  $200^\circ$  produces a more systematic variation in the STF durations). We checked STF estimates obtained without using the positivity constraint applied to the signals

We tested five models (Table 1), including both nodal planes of the GCMT focal mechanisms for this event, the preferred orientation of Kaverina et al. [1998], a  $200^\circ$  striking plane as indicated by the R1 STF observations, and a plane with the megathrust geometry of the events in the 2009 sequence. For all models, we used a rupture speed of 2.0 km/s and subfault source time

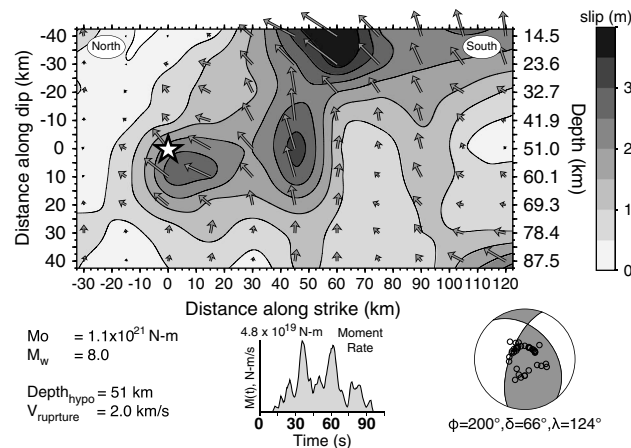


**Figure 10.** Finite-fault model from a kinematically constrained linear least squares inversion of teleseismic *P* and *SH* waves for the 1997 event. Here we show the model found for the steeply dipping nodal plane of the GCMT solution, but with a strike of 200° as indicated by analysis of the STFs (Figure 9) (waveform comparisons are shown in Figure S2). All models display a similar characteristic of small slip near the hypocenter and peak slip at shallow depth, correlating with the region of concentrated aftershock activity. The arrows indicate the rake and relative slip amplitude for each subfault. The black circles within the lower hemisphere focal mechanism indicate takeoff angles and azimuths to stations used in the inversion.

In case, the mechanism is fixed and the point source subevents are inverted for their location along the fault plane (along strike and dip), seismic moment, and onset time. In the second method, the inversion allows variable faulting geometry among subevents. In this case, the sources are identified by their location along strike and dip, moment, onset time, and focal mechanism. Using a fixed mechanism similar to that used in the finite-fault modeling and four subevents, the KK model shows general agreement with slip patterns from the finite-fault model (Figures 11 and S3). Allowing the focal parameters to vary among subevents, the KK model includes significant variation between the subevents (Figures 11 and S4). Strike for the subevents varies from ~90° to 180°. Rake also varies, with one subevent ~40 km south of epicenter having a rake significantly rotated from the rest of the subevents. For this event, both the fixed and variable mechanism models provide similar quality fits to the data. Clearly, the data do not allow us to unambiguously demonstrate that the 1997 event ruptured a near-vertical fault within the downgoing slab, but we note that such a model is compatible with the deep centroid estimates, R1 STFs, and the body wave constraints.

### 5. The 2013 Vanuatu Earthquake

Several analyses of the 2013 sequence have been reported. *Lay et al.* [2013] used similar methods to those applied here but also included modeling of tsunami observations. *Hayes et al.* [2014] also studied the rupture process but focused more on the foreshock and aftershock sequence and the possible relationship between the 2013 earthquake and a postulated slow-sliding event along its southern margin that may have influenced the aftershock activity. For completeness, we investigate characteristics of the event using the same approaches that we applied to the other large Vanuatu events. As noted in *Lay et al.* [2013], R1 STFs provide some insight into the 2013 rupture (Figure 12). For the STF estimation, we assumed a point source consistent with the GCMT faulting geometry ( $\phi = 314^\circ$ ,  $\delta = 21^\circ$ , and  $\lambda = 74^\circ$ ) and a depth of 27 km. We aligned the signals by handpicking the STF onsets. The R1 STFs for the 2013 event display pulse durations ranging from ~75 to 140 s, with an average duration of ~105 s. The duration does not vary uniformly with azimuth; some signals with the same directivity parameter display durations shorter than others. This may indicate complexity in the rupture directivity, with a rupture that may have propagated in multiple directions. However, the dominant trend of the STF durations indicates rupture toward an azimuth of ~135°. Assuming an R1 phase velocity of 4 km/s, the 62 s of directivity suggests a rupture length of ~125 km; the estimated rupture speed is ~1.5 km/s. These results are consistent with those of *Lay et al.* [2013].

functions were parameterized by 10 half-overlapping triangles with widths of 2.0 s. Smoothing was applied to generate the simplest model that produces an acceptable fit to the observations. All of the orientations provide comparable fits to the waveforms, with all geometries accounting for 75–85% of the observed, complicated waveforms (Figure S2). Figure 10 shows the slip model for the geometry with a strike of 200° as indicated by the R1 STFs with a steeply dipping nodal plane like that for the GCMT solution. As in this figure, all of the models that we considered place substantial slip shallow and near the region of dense aftershocks.

For additional insight into the 1997 event's rupture complexity, we used a more flexible iterative deconvolution method [*Kikuchi and Kanamori, 1982*] (KK approach). The KK approach iteratively models an earthquake source as a series of double-couple point sources. We explored two types of inversion. In one

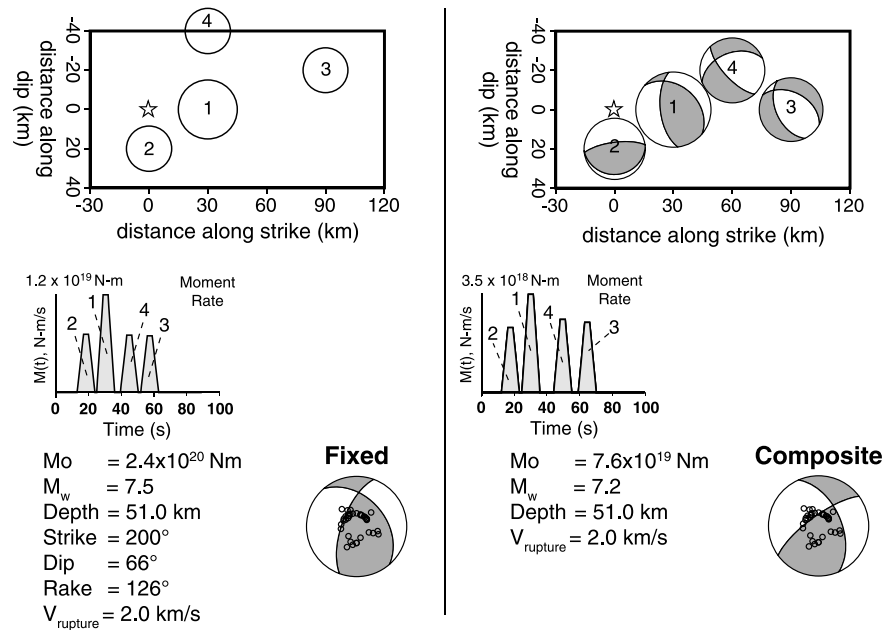


**Figure 11.** Kikuchi-Kanamori iterative deconvolution models [Kikuchi and Kanamori, 1982] for the 1997 main shock for a (left) fixed (waveform comparisons are shown in Figure S3) and (right) variable mechanisms (waveform comparisons are shown in Figure S4). Both models use the same hypocenter depth as for the finite-fault model (Figure 10) and four subevent iterations. Results for the fixed mechanism show the location of the subevents on the rupture plane. Results for the variable mechanism inversion show the location of each subevent along strike. A star locates the event hypocenter. Below the subevents is the composite mechanism for the entire event. The contribution of each subevent to the moment rate function is labeled.

Finite-fault modeling provides a more detailed rupture analysis, demonstrating that the 2013 event ruptured with a two-patch slip pattern (Figures 13 and S5). The GCMT and NEIC centroid moment tensor solutions ( $\phi = 311^\circ$ ,  $\delta = 28^\circ$ ,  $\lambda = 68^\circ$ , and depth = 32 km) are problematic because given the hypocenter at this depth, the dip of a single-plane fault model results in a rupture plane  $\sim 10$  km below the surface at the trench. Tsunami modeling by Lay *et al.* [2013] suggests that the rupture extended to shallow depths, requiring a shallower hypocenter, steeper dip, or southwestward event mislocation. The NEIC W-phase moment tensor solution is similar to the GCMT solution ( $\phi = 309^\circ$ ,  $\delta = 17^\circ$ , and  $\lambda = 61^\circ$ ); however, the shallower hypocenter depth (depth = 15 km) places the fault plane at a physically reasonable depth at the trench.

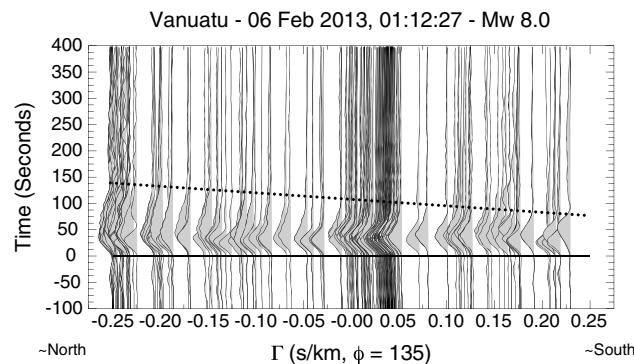


**Figure 12.** R1 source time functions (STFs) for the 2013 main shock earthquake plotted versus directivity parameter,  $\Gamma$ , for an assumed rupture azimuth of  $135^\circ$ . The rupture appears to propagate to the southeast with an estimated rupture speed of about 1.5 km/s and an  $\sim 105$  s duration.

For our finite-fault modeling, we produced a good fit to the *P* and *SH* waves with a faulting geometry similar to the U.S. Geological Survey (USGS) W-Phase moment tensor solution ( $\phi = 309^\circ$ ,  $\delta = 17^\circ$ , and  $\lambda = 58^\circ$ ). We fixed the epicenter to the NEIC location but decreased the hypocenter depth to bring the fault near the surface at the trench ( $10.738^\circ\text{S}$ ,  $165.138^\circ\text{E}$ , 18 km). We also tested a deeper source of 28.7 km, but with a slightly steeper dip than the GCMT and NEIC centroid moment tensor solutions ( $\phi = 309^\circ$ ,  $\delta = 30^\circ$ , and  $\lambda = 58^\circ$ ) in order to place the fault plane near the surface at the trench. While both models produced a similar slip pattern, we will focus on the model with a shallower hypocenter as

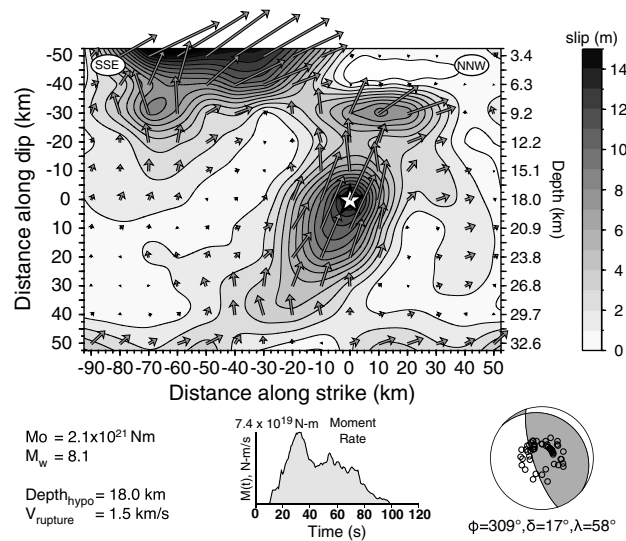


**Figure 13.** Finite-fault model from a kinematically constrained linear least squares inversion of teleseismic *P* and *SH* waves for the 2013 event. Here we show the model for a shallow hypocenter (18 km) with shallowly dipping plane (dip = 17°) (Waveform comparisons are shown in Figure S5.). Inversion results for a deeper hypocenter with the same dip are shown in Figures S6 and S7 and for a deeper hypocenter with steeper dip in Figures S8 and S9. All models display a similar characteristic of large slip near the hypocenter and peak slip at shallow depth to the south-southeast. While peak slip occurs shallow on the fault plane where the shear modulus is low, the peak moment is located near the hypocenter (Figure S10). The difference is from the change in shear modulus with depth.

near the hypocenter (Figure S10) (the Earth model shear modulus increases with depth). The model rupture length is compatible with the rupture length estimation of ~120 km from the STF analysis. The finite-fault model's moment rate function is also consistent with the results of the STF analysis. The 2013 event moment rate function has a relatively simple triangular shape with a duration of ~90 s, but again, the large moment of this model suggests that constraining the long-period components of the STF with only body waves can be difficult. The moment rate function begins with a ~20 s rise time to peak slip, and rupture continued for about 70 s following the peak moment, with moment rate remaining nearly constant between 30 and 60 s after initiation. This model has a centroid at 10.88°S, 165.28°E, and depth = 17 km, which is ~25 km northeast and shallower than the GCMT centroid (11.08°S, 165.14°E, and depth = 27.6 km). The model's temporal centroid is 34.2 s, ~6 s larger than the GCMT value. The R1 STFs suggest rupture nearly parallel to the strike of the trench ( $\phi = 135^\circ$ ), while the finite-fault model would suggest directivity closer to ~180°. However, it is possible that when the rupture reached the top of the fault plane, propagation then proceeded along strike. Low-frequency energy radiated from this shallow portion of the plate boundary may have dominated the R1 signals, suggesting there may have been some depth-dependent frequency dependence during the event [e.g., Ishii, 2011; Koper et al., 2011a, 2011b, 2012; Lay et al., 2012].

We found evidence for a depth dependence in the frequency content of seismic radiation from larger earthquakes [Lay et al., 2012] using the KK iterative inversion approach. Results from the fixed and variable mechanism inversions, using faulting parameters similar to those used in the finite-fault modeling, identify subevents near and downdip of the hypocenter (Figures 14 and S11–S15). These inversions do not resolve the very shallow slip found in the finite-fault modeling. The finite-fault inversion procedure has greater flexibility to vary subfault source time functions, which may play a role in why it resolves shallow longer-duration slip better than the iterative inversion methods. For the variable mechanism pulse-stripping inversion, we limited the number of subevents to four, as the model began to show instability for more (strongly diverse faulting geometry for each subevent). Three of the four subevents in this model had faulting geometry generally similar to that of the GCMT. The fourth subevent, however,

it provides a slightly improved fit to the waveforms. We note, however, that the steeper dip is more similar to the dip of the 1980 and 2009 events to the south. Models with a deeper source or steeper dip are shown in Figures S6–S9.

As indicated by the R1 STF analysis, the observed waveforms are best fit using a relatively slow rupture velocity of 1.5 km/s. The model's seismic moment,  $2.12 \times 10^{21}$  N m, is higher than the GCMT estimate of  $8.65 \times 10^{20}$  N m. Only a modest smoothing constraint was needed to stabilize the inversion. The model hypocenter is located in the middle of a region of high slip. Two other relatively large slip regions are located updip, with most slip occurring at shallow depth and slightly south of the hypocenter (similar to the models in Lay et al. [2013], which provided good fits to tsunami observations that are particularly sensitive to the shallow slip). The model includes modest slip extending 30 km downdip and 30 km north of the hypocenter. While maximum slip occurs at shallow depths, the maximum seismic moment is located

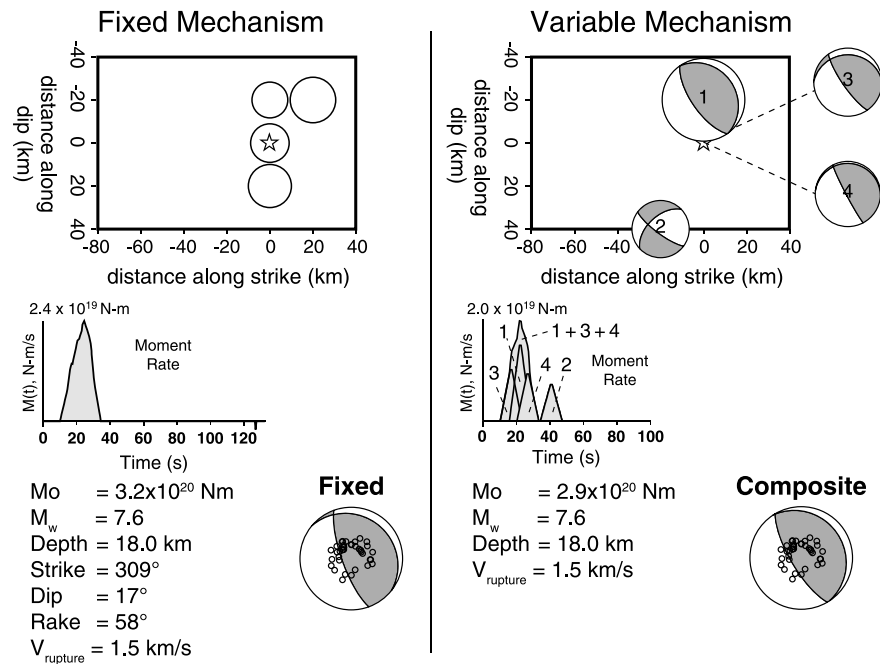


**Figure 14.** Kikuchi-Kanamori iterative deconvolution models [Kikuchi and Kanamori, 1982] for a (left) fixed (waveform comparisons are shown in Figure S11) and (right) variable mechanisms (waveform comparisons are shown in Figure S12) of the 2013 main shock. Both inversion models use a shallow hypocenter (18 km), similar to that used in the finite-fault model (Figure 13) and four subevents. Results for the fixed mechanism show the location of the subevents on the rupture plane. A star locates the event hypocenter. This model does not resolve the shallow slip observed in the finite-fault model. Results for the variable mechanism inversion show the location of each subevent along strike. The second subevent is located along the lower boundary of the rupture plane; the third and fourth subevents are both located at the same location as the hypocenter. Below the subevents is the total mechanism for the entire event as a whole. The contribution of each subevent to the moment rate function is labeled. Additional iterative deconvolution models assuming a deeper hypocenter and more steeply dipping fault plane are shown in Figures S13–16.

has a substantially different rake, making the subevent nearly strike slip, located south and downdip of the hypocenter.

The 2013 main shock (Figure 15) ruptured to the north of the 1966 sequence and exhibited clear differences from the 1980, 1997, and 2009 events in terms of the foreshock distribution, and faulting mechanisms of foreshocks/aftershocks. The 2013 earthquake was preceded by abundant moderate-to-large foreshocks; there were seven  $M \geq 6.0$  foreshocks in the 100 days prior to the 2013 event. No other event that we analyzed had such a vigorous foreshock sequence over a similar time period prior to the initial main shock. Based on the ISC catalog, no significant foreshock activity preceded the 1966 earthquake. For the 2013 event, the 1 month foreshock activity was isolated near the epicenter of the main shock and in a tight cluster of shallow seismicity  $\sim 30$  km east of Nendō Island. The 1 month aftershock zone indicates that the rupture was compact. Overall, the aftershocks suggest that the event activated the plate boundary from the northern “corner” at  $\sim 10.5^\circ\text{S}$  to about 100 km to the south. This zone is approximately half of the size of that of the largest 1980 and 2009 events (Figure 2), which is surprising considering the 2013 event had a 50% larger seismic moment than that of the larger 2009 event. The 2013 aftershock zone extended through the region from  $11^\circ\text{S}$  to  $11.5^\circ$  that had aftershocks in the 1966, 1980, and 2009 sequences but did not extend into the large-slip zone of the 1966 event.

The mechanisms of the foreshocks/aftershocks for the 2013 event also differ from those for the 1980, 1997, and 2009 events. Based on NEIC hypocenters and GCMT moment tensors, the seismicity associated with the events in 1980, 1997, and 2009 appeared to largely occur along the megathrust. The foreshocks and aftershocks of the 2013 event appear to have occurred on many different structures [Hayes et al., 2014]. The event was followed by three shallow  $M_w \geq 7.0$  events in the 2 days after the main shock [Hayes et al., 2014].

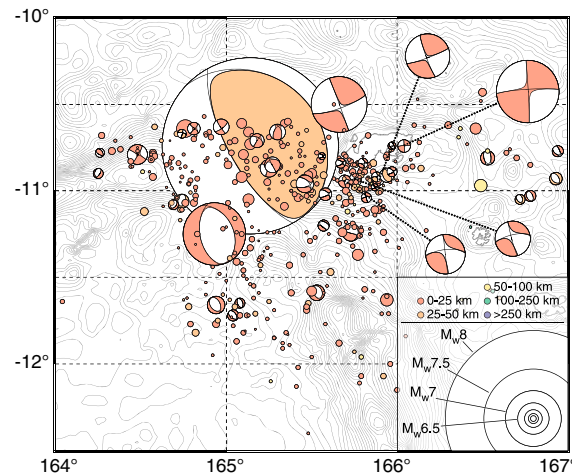


**Figure 15.** Forty day aftershock sequence for the 2013 earthquake, including all events listed in the NEIC catalog. Focal mechanisms are located and scaled to the NEIC catalog information. Nineteen of the largest events (not including the main shock) were relocated using surface waves [Cleveland and Ammon, 2013] (Table S1).

These three events included a normal-faulting  $M_w$  7.1 in the outer rise (NEIC: 6 February 2013 01:23:20 UTC, 11.254°S 164.932°E) and two strike-slip events to the east of the main shock, near Nendö Island (NEIC:  $M_w$  7.0, 10.479°S 165.772°E, 6 February 2013 01:54:15 UTC;  $M_w$  7.1, 10.932°S 166.021°E, 8 February 2013 15:26:38 UTC). There was also shallow normal faulting ~50 km east of Nendö Island, and the plate boundary west of the northern corner of the arc was also activated with seismicity of various faulting geometries (Figure 15). While the abundance of off-megathrust seismicity was absent from the three prior large sequences, the foreshock/aftershock seismicity east of Nendö Island was also observed in the 1966 sequence (Figure 2).

The complex 2013 foreshock/aftershock behavior is likely due to the tectonic setting near the northern limit of the Vanuatu subduction zone and corner of

the Australian-Pacific Plate boundary. Just north of the 2013 hypocenter, the Australian plate transitions from a near west-east oriented strike-slip plate boundary west of the corner, into a near north-south oriented convergent boundary south of the corner as it subducts beneath the Pacific Plate. Consequently, downdip of the northern limit of the subduction zone is the edge of the Australian plate, with subducted material to the south and none to the north. Hayes et al. [2014] interpret the 2013 aftershocks that exhibit right-lateral slip to be indicative of block-like motion within the overriding plate.

## 6. Discussion

We estimated finite-fault models for three earthquakes: the 1997 ( $M_w$  7.7), the first 2009 ( $M_w$  7.6), and the 2013 ( $M_w$  8.0) events. These large earthquakes appear to be characterized by ~50 km dimension patches of strong slip that may represent frictional or structural

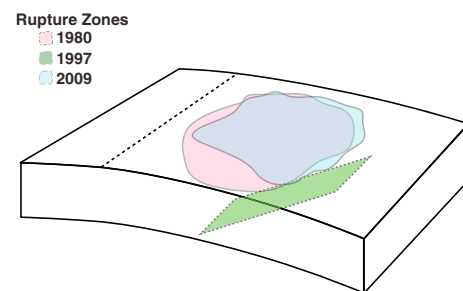


**Figure 16.** Schematic showing the spatial relationships of the 1980, 1997, and 2009 large earthquake ruptures in northern Vanuatu. We interpret the 1997 event as an intraplate rupture based on a collective assessment of broadband seismic observations (ambiguous broadband  $P$  waveforms, unusual faulting geometry, deep long-period centroid, and unusual aftershock spatial relationships). Due to limited waveform data, we are unable to constrain precisely how much the 1980 and 2009 rupture zones overlapped. However, analysis of available waveforms indicates that the 2009 sequence was not an exact repeat of the 1980 sequence (Figure 8).

heterogeneities along the megathrust. Our model for the 2013 main shock is generally consistent with those detailed in Lay et al. [2013] and Hayes et al. [2014]. The event had two regions of high slip, including one with very large slip near the trench. Lay et al. [2013] related the large, shallow slip to tsunamigenesis. Since the slip of the 2013 event is detailed in Lay et al. [2013] and Hayes et al. [2014], we focus on the 2009 and 1997 events.

The 2009 sequence appears to have reruptured much of the same region of the megathrust as the 1980 sequence (Figure 16). Long-period signals indicate a similarity of the 1980 and 2009 sequences, but the differences in relative seismic wave amplitudes also indicate that the 2009 sequence was not an exact repeat of the 1980 sequence (Figure 8). We are confident that the two sequences overlapped along the trench axis (Figure 2), but we cannot precisely constrain the overlap. Whether the difference is related to overlapping along-strike interactions or predominantly represents a downdip combination of asperities is difficult to discern given the data available for 1980. The  $m_b/M_w$  ratios (Table 2) of

**Table 2.** Large Northern Vanuatu Earthquakes Investigated in This Study

Date	Hypocenter <sup>a</sup>			Magnitude				Focal <sup>b</sup> (°)		
	Latitude (°S)	Longitude (°E)	Depth (km) <sup>a</sup>	Moment (dyn-cm) <sup>b</sup>	$M_w^{a,b}$	$m_b^b$	$M_s^b$	Strike	Dip	Rake
8 Jul 1980 23:19:19.8	12.41	166.38	33	1.97E + 27	7.8,7.5	5.9	7.5	353	49	100
17 Jul 1980 19:42:23.2	12.52	165.92	33	4.84E + 27	8.0,7.7	5.8	7.9	351	31	102
21 Apr 1997 12:02:26.4	12.58	166.68	33	4.39E + 27	7.7,7.7	6.4	7.9	301	39	40
7 Oct 2009 22:03:14.5	13.01	166.51	45	3.27E + 27	7.7,7.6	6.4	7.7	344	41	87
7 Oct 2009 22:18:51.2	12.52	166.38	35	6.67E + 27	7.8,7.8	6.4	7.9	337	36	82
7 Oct 2009 23:13:48.2	13.09	166.5	31	1.65E + 27	7.4,7.4	6.4	7.4	341	43	83
6 Feb 2013 21:12:27.0	10.74	165.14	29	9.37E + 27	8.0,7.9	6.4	8.0	320	20	89

<sup>a</sup>National Earthquake Information Center catalog.

<sup>b</sup>Global Centroid Moment Tensor catalog.

the 1980 events are substantially lower than those of the 2009 and 2013 events, suggesting that the 1980 events may have been relatively deficient in short-period radiation. The short-period deficiency may indicate that the rupture was shallower [e.g., *Ishii*, 2011; *Koper et al.*, 2011a, 2011b, 2012; *Lay et al.*, 2012]. Thus, the 1980 and 2009 sequences likely included rupture of overlapping regions that either failed in a different order, represent different mixes of asperities, or probably included more shallow slip in 1980.

The 1997 sequence shows the complex nature of plate interactions in the region. Body wave relocation places the 1997 hypocenter deeper, arcward, and between the first and second 2009 events. However, the detectable 1997 aftershock activity was localized near the trench, south of the southern limit of the 1980 sequence, and close to the third 2009 event (Figures 2 and 17). The 1997 GCMT is closer to the aftershock activity near the trench (13.21°S, 166.20°E). A relatively large tsunami was associated with this event, suggesting that the rupture may have reached shallow depths. We cannot confidently identify the rupture geometry for the 1997 event. The centroid locations, body wave, and R1 directivity analyses of the 1997 event suggest that the rupture began deep and in the north then propagated ~80 km south and toward the trench where much of the slip occurred (consistent with the robust features in the model of *Kaverina et al.* [1998]). Despite the occurrence of 1997 event, the segment of the megathrust trenchward of its hypocenter remained strained, rupturing 12 years later during the 2009 sequence. Partially for this reason, our preferred interpretation of the 1997 event is an intraplate event within the subducting plate.

Since 1963, 9 of the 15 northern Vanuatu earthquakes with  $M \geq 7.5$  occurred in doublet sequences (Table 3). *Felzer et al.* [2004] concluded that the global occurrence of doublets is in accord with the statistics expected from a physical rupture model based on a single triggering event, but this generality does not account for spatial clustering of doublets in regions such as northern Vanuatu. The high proportion of large doublet events in the region suggests that effective triggering of nearby asperities plays an important role in seismic strain release along this plate boundary. However, doublets have not been identified in northern Vanuatu between 1900 and 1963. Some doublets with short interevent times, like for the largest 2009 pair, could have been misinterpreted as a single event, but pairs of events even an hour apart would likely have been noted. The lack of evidence for doublets in the early 1990s may indicate that the characteristic varies with time.

Additional evidence for asperity interaction in the northern Vanuatu comes from aftershock zone expansion [*Tajima and Kanamori*, 1985]. The recent activity provides more information on the process. Each aftershock sequence provides clues to dynamic aftershock triggering throughout the region (Figure 2). The 1966 and 2013 events included a number of foreshock and aftershocks in the back-arc region and produced widespread aftershocks in the north but did not trigger events in the 1980–2009 rupture regions. While both the 1980 and 2009 sequences triggered events in the north, the 2009 sequence appears to have activated more  $M_w$  4–5.5 seismicity than the 1980 sequence (Figures 2 and 17). The difference may be in part due to small-event detection improvement since 1980 but could also indicate that the northern region had a reduced stress level following the 1966 sequence, which had ruptured and produced widespread aftershocks in the north (Figure 2). A similar reduced stress state (caused by the 2009 sequence) could also be interpreted from the lack of triggering of events in the south by the 2013 event. Prior to 2009, the 1997 event triggered aftershocks throughout the region that eventually failed in 2009. The fact that both 2009 and 2013 triggered seismicity in the former 1966 rupture area suggests that this region may have recovered much of the strain released in 1966.

**Table 3.** Northern Vanuatu Events  $M > 7.5$  Since 1960

Date <sup>a</sup>	Hypocenter <sup>a</sup>			Magnitude		
	Latitude (°S)	Longitude (°E)	Depth (km)	$M_w$	$m_b$ <sup>b</sup>	$M_s$ <sup>b</sup>
15 Sep 1963 00:46:54.0 <sup>f</sup>	10.47 <sup>f</sup>	165.76 <sup>f</sup>	35 <sup>f</sup>	7.5 <sup>f</sup>	—	—
17 Sep 1963 19:20:11.0 <sup>f</sup>	10.28 <sup>f</sup>	165.41 <sup>f</sup>	29.5 <sup>f</sup>	7.5 <sup>f</sup>	—	—
20 May 1965 00:40:12.0 <sup>f</sup>	14.64 <sup>f</sup>	167.50 <sup>f</sup>	9.7 <sup>f</sup>	7.6 <sup>f</sup>	—	—
31 Dec 1966 18:23:08.8 <sup>c</sup>	11.90 <sup>c</sup>	166.40 <sup>c</sup>	56 <sup>d</sup>	7.5 <sup>d</sup>	7.3 <sup>f</sup> , 5.5 <sup>d</sup>	7.9 <sup>d</sup>
31 Dec 1966 22:15:17.1 <sup>c</sup>	12.10 <sup>c</sup>	165.70 <sup>c</sup>	—	7.2 <sup>f</sup>	—	7.3 <sup>d</sup>
11 Aug 1970 10:22:20.0 <sup>e</sup>	14.12 <sup>e</sup>	166.65 <sup>e</sup>	33 <sup>c</sup>	7.5 <sup>e</sup>	6.2 <sup>e</sup>	7.0 <sup>e</sup>
28 Dec 1973 13:41:45.8	14.46	166.60	26	7.3 <sup>a</sup> , (7.8 <sup>g</sup> )	—	7.5 <sup>h</sup>
8 Jul 1980 23:19:19.8	12.41	166.38	33	(7.8 <sup>g</sup> ), 7.5 <sup>b</sup>	5.9	7.5
17 Jul 1980 19:42:23.2	12.52	165.92	33	(8.0 <sup>g</sup> ), 7.7 <sup>b</sup>	5.8	7.9
5 Aug 1982 20:32:52.9	12.60	165.93	30	7.1 <sup>h</sup> , 6.9 <sup>b</sup>	6.2	7.1, 7.5 <sup>g</sup>
28 Nov 1985 03:49:54.1	13.99	166.18	33	7.0 <sup>f</sup> , 7.0 <sup>b</sup>	6.2	7.1, 7.6 <sup>g</sup>
21 Dec 1985 01:13:22.4	13.97	166.52	43	7.1 <sup>f</sup> , 7.1 <sup>b</sup>	6.1	7.3, 7.6 <sup>g</sup>
21 Apr 1997 12:02:26.4	12.58	166.68	33	7.7 <sup>a</sup> , 7.7 <sup>b</sup>	6.4	7.9
7 Oct 2009 22:03:14.5	13.01	166.51	45	7.7 <sup>a</sup> , 7.6 <sup>b</sup>	6.4	7.7
7 Oct 2009 22:18:51.2	12.52	166.38	35	7.8 <sup>a</sup> , 7.8 <sup>b</sup>	6.4	7.9
6 Feb 2013 21:12:27.0	10.74	165.14	29	8.0 <sup>a</sup> , 7.9 <sup>b</sup>	6.4	8.0

<sup>a</sup>National Earthquake Information Center catalog.  
<sup>b</sup>Global Centroid Moment Tensor catalog.  
<sup>c</sup>Tajima et al. [1990].  
<sup>d</sup>United State Earthquake catalog.  
<sup>e</sup>California Geologic Survey catalog.  
<sup>f</sup>Centennial catalog [Engdahl and Villaseñor, 2002].  
<sup>g</sup>Berkeley (BRK), () indicates UK magnitude scale.  
<sup>h</sup>USGS-NEIC.

Asperity interaction was originally proposed as an explanation for large doublets in the Solomon Islands [Lay and Kanamori, 1980] and aftershock expansion patterns. Aftershock expansion characteristics led Tajima and Kanamori [1985] to suggest that the northern Vanuatu megathrust hosts numerous, interacting moderate-sized (up to 50 km dimension) asperities. Tajima and Kennett [2012] generalized the idea and categorized major subduction zones based upon their aftershock expansion patterns. In the model, regions such as northern Vanuatu that exhibit large aftershock expansion are unlikely capable of producing events with magnitudes much larger than 8.0. Our new observations support these ideas. The similarities and differences of the 1980 and 2009 events, the tendency for failure in large doublets, and the expansion of

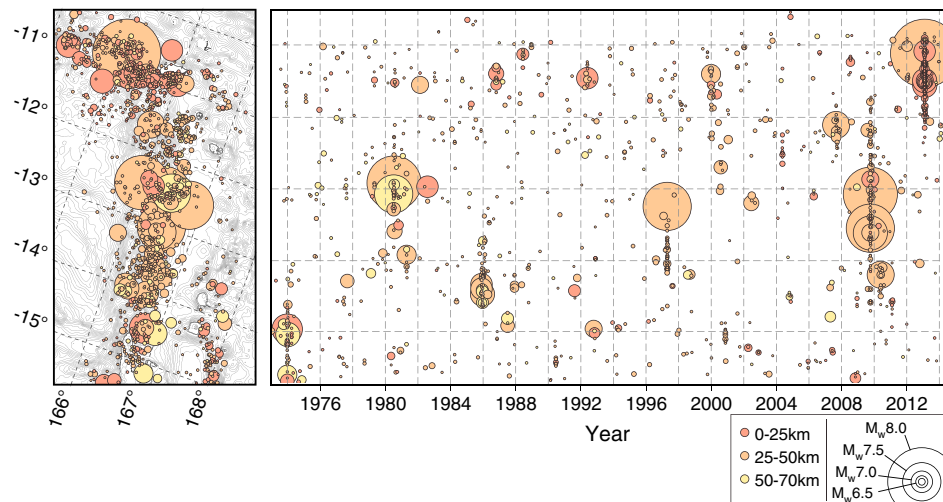


**Figure 17.** (right) Space-time plot of shallow ( $\leq 70$  km) seismicity  $M \geq 5.0$  in northern Vanuatu recorded in the NEIC catalog as a function of distance south of  $-10^\circ\text{N}$ ,  $165.25^\circ\text{E}$ . (left) The location of the seismicity on a map rotated to orient the trench vertically.

aftershock regions suggest that the northern Vanuatu megathrust contains numerous, moderate-sized asperities that interact to produce frequent large earthquakes. Although the possibility of the seismic cycles synchronizing and rupture propagating across broad regions of asperities cannot be ruled out, consistent with the model of *Tajima and Kennett* [2012], northern Vanuatu is unlikely to fail in a single megathrust event.

## 7. Conclusion

Recent large earthquakes in the northern Vanuatu subduction zone have occurred in several sequences that have ruptured almost all of the megathrust from 10.5°S to 13.5°S. The 2009 sequence ruptured the same general region as the 1980 doublet; however, differences in waveforms suggest that there are some differences in the rupture areas of the events. The 1997 event nucleated deeper than the earlier large 1980 events, ruptured oblique to the trench, and produced substantial aftershock activity in a region roughly coincident with the third event in the 2009 sequence. The 1997 event may be intraplate, within the underthrusting Australian plate. The 1966 and 2013 events ruptured fault segments north of the other large events. The 2013 event rupture appears to have extended to the trench, had regions of very high (> 10 m) slip, and included strong low-frequency radiation, possibly reflecting depth dependence in the frequency content of seismic radiation. The rapid expansion of aftershock area following the 1966, 1980, and 2009 earthquakes, the frequent large doublets, and the reconfiguration of asperities involved in the 1980 and 2009 sequences suggest that the failure mode in northern Vanuatu is dominated by moderate-sized asperity interaction.

## Acknowledgments

We thank the Defense Threat Reduction Agency for partial support under Award HDTRA1-11-1-0027 (K.M.C.). K.M.C. performed revisions of this work under the auspices of the Department of Energy for the Los Alamos National Laboratory under the contract DE-AC52-06NA25396. T.L. is supported by NSF grant EAR1245717. We acknowledge the staff and support provided to the IRIS/USGS GSN and Global Centroid Moment Tensor (CMT). Global Seismographic Network (GSN) is a cooperative scientific facility operated jointly by the Incorporated Research Institutions for Seismology (IRIS), the United States Geological Survey (USGS), and the National Science Foundation (NSF). The facilities of the IRIS Data Management System, and specifically the IRIS Data Management Center, were used for access to waveform and metadata required in this study. The IRIS DMS is funded through the NSF and specifically the GEO Directorate through the Instrumentation and Facilities Program of the NSF under Cooperative Agreement EAR-1063471. Waveform data used in this study are available through the IRIS Data Management System. Earthquake event information is found in NEIC and GCMT earthquake catalogs. We also thank all those who openly share large earthquake data recorded on their seismic networks. Thanks also to the developers of SAC [Goldstein et al., 2003] and GMT [Wessel and Smith, 1998]. Finally, we thank the two reviewers for their constructive criticism that greatly improved this paper.

## References

- Abercrombie, R. E., M. Antolik, and G. Ekström (2003), The June 2000  $M_w$  7.9 earthquakes south of Sumatra: Deformation in the India-Australia Plate, *J. Geophys. Res.*, *108*(B1), 2018, doi:10.1029/2001JB000674.
- Allen, T. I., K. Marano, P. S. Earle, and D. J. Wald (2009), PAGER-CAT: A composite earthquake catalog for calibrating global fatality models, *Seismol. Res. Lett.*, *80*(1), 50–56.
- Ammon, C. J., A. A. Velasco, and T. Lay (2006), Rapid estimation of first-order rupture characteristics for large earthquakes using surface waves: 2004 Sumatra-Andaman earthquake, *Geophys. Res. Lett.*, *33*, L14314, doi:10.1029/2006GL026303.
- Ammon, C. J., H. Kanamori, and T. Lay (2008), A great earthquake doublet and seismic stress transfer cycle in the central Kuril islands, *Nature*, *451*(7178), 561–565.
- Cleveland, K. M., and C. J. Ammon (2013), Precise relative earthquake location using surface waves, *J. Geophys. Res. Solid Earth*, *118*, 2893–2904, doi:10.1002/jgrb.50146.
- DeMets, C., R. G. Gordon, and D. F. Argus (2010), Geologically current plate motions, *Geophys. J. Int.*, *181*, 1–80.
- Ekström, G., M. Nettles, and A. M. Dziewonski (2012), The global CMT project 2004–2010: Centroid-moment tensors for 13,017 earthquakes, *Phys. Earth Planet. Inter.*, *200–201*, 1–9.
- Engdahl, E. R., and A. Villaseñor (2002), Global seismicity: 1900–1999, in *International Handbook of Earthquake and Engineering Seismology*, Part A, chap. 41, edited by W. H. K. Lee et al., pp. 665–690, Academic Press, London.
- Felzer, K. R., R. E. Abercrombie, and G. Ekström (2004), A common origin for aftershocks, foreshocks, and multipllets, *Bull. Seismol. Soc. Am.*, *94*(1), 88–98.
- Goldstein, P., D. Dodge, M. Firpo, and L. Minner (2003), SAC2000: Signal processing and analysis tools for seismologists and engineers, in *The IASPEI International Handbook of Earthquake and Engineering Seismology, International Geophysics Series*, part B, vol. 81, edited by W. H. K. Lee et al., pp. 1613–1614, Academic Press, London, U. K.
- Hayes, G. P., K. P. Furlong, H. M. Benz, and M. W. Herman (2014), Triggered aseismic slip adjacent to the 6 February 2013  $M_w$  8.0 Santa Cruz Islands megathrust earthquake, *Earth Planet. Sci. Lett.*, *388*, 265–272.
- Houston, H., H. Anderson, S. L. Beck, J. Zhang, and S. Schwartz (1993), The 1986 Kermadec earthquake and its relation to plate segmentation, *Pure Appl. Geophys.*, *140*(2), 331–364.
- Ishii, M. (2011), High-frequency rupture properties of the  $M_w$  9.0 off the Pacific coast of Tohoku earthquake, *Earth Planets Space*, *63*, 609–6014.
- Kagan, Y. Y., and D. D. Jackson (1999), Worldwide doublets of large shallow earthquakes, *Bull. Seismol. Soc. Am.*, *89*(5), 1147–1155.
- Kaverina, A., D. Dreger, and M. Antolik (1998), Source process of the 21 April, 1997 Santa Cruz Island earthquake ( $M_w$  7.8), *Geophys. Res. Lett.*, *26*(21), 4027–4030, doi:10.1029/1998GL900017.
- Kikuchi, M., and H. Kanamori (1982), Inversion of complex body waves, *Bull. Seismol. Soc. Am.*, *72*, 491–506.
- Koper, K. D., A. R. Hutko, T. Lay, C. J. Ammon, and H. Kanamori (2011a), Frequency-dependent rupture process of the 2011  $M_w$  9.0 Tohoku Earthquake: Comparison of short-period  $P$  wave backprojection images and broadband seismic rupture models, *Earth Planets Space*, *63*, 599–602.
- Koper, K. D., A. R. Hutko, and T. Lay (2011b), Along-dip variation of teleseismic short-period radiation from the 11 March 2011 Tohoku earthquake ( $M_w$  9.0), *Geophys. Res. Lett.*, *38*, L21309, doi:10.1029/2011GL049689.
- Koper, K. D., A. R. Hutko, T. Lay, and O. Sufri (2012), Imaging short-period seismic radiation from the 27 February 2010 Chile ( $M_w$  8.8) earthquake by back-projection of  $P$ ,  $PP$ , and  $PKIKP$  waves, *J. Geophys. Res.*, *117*, B02308, doi:10.1029/2011JB008576.
- Lay, T., and H. Kanamori (1980), Earthquake doublets in the Solomon Islands, *Phys. Earth Planet. Inter.*, *21*(4), 283–304.
- Lay, T., C. J. Ammon, H. Kanamori, L. Rivera, K. D. Koper, and A. R. Hutko (2010a), The 2009 Samoa-Tonga great earthquake triggered doublet, *Nature*, *466*(7309), 964–968.
- Lay, T., C. J. Ammon, A. R. Hutko, and H. Kanamori (2010b), Effects of kinematic constraints on teleseismic finite-source rupture inversions: Great Peruvian earthquakes of 23 June 2001 and 15 August 2007, *Bull. Seismol. Soc. Am.*, *100*(3), 969–994.
- Lay, T., H. Kanamori, C. J. Ammon, K. D. Koper, A. R. Hutko, L. Ye, H. Yue, and T. M. Rushing (2012), Depth-varying rupture properties of subduction zone megathrust faults, *J. Geophys. Res.*, *117*, B04311, doi:10.1029/2011JB009133.

- Lay, T., L. Ye, H. Kanamori, Y. Yamazaki, K. F. Cheung, and C. J. Ammon (2013), The February 6, 2013  $M_w$  8.0 Santa Cruz Islands earthquake and tsunami, *Tectonophysics*, *608*, 1109–1121.
- Tajima, F., and H. Kanamori (1985), Aftershock area expansion and mechanical heterogeneity of fault zone within subduction zones, *Phys. Earth Planet. Inter.*, *12*(6), 345–348.
- Tajima, F., and B. L. N. Kennett (2012), Interlocking of heterogeneous plate coupling and aftershock area expansion pattern for the 2011 Tohoku-Oki  $M_w$ 9 earthquake, *Geophys. Res. Lett.*, *39*, L05307, doi:10.1029/2011GL050703.
- Tajima, F., L. J. Ruff, H. Kanamori, J. J. Zhang, and K. Y. Mogi (1990), Earthquake source processes and subduction regime in the Santa Cruz Islands region, *Phys. Earth Planet. Inter.*, *61*, 269–290.
- Utsu, T., and A. Seki (1954), Relation between the area of aftershock region and the energy of the main shock [in Japanese], *J. Seismol. Soc. Jpn*, *7*, 233–240.
- Waldhauser, F., and W. L. Ellsworth (2000), A double-difference earthquake location algorithm; method and application to the northern Hayward Fault, California, *Bull. Seismol. Soc. Am.*, *90*(6), 1353–1368.
- Wessel, P., and W. H. F. Smith (1998), New, improved version of Generic Mapping Tools released, *Eos Trans. AGU*, *79*, 579, doi:10.1029/98EO00426.